Optical Engineering

OpticalEngineering.SPIEDigitalLibrary.org

Modeling satellite-Earth quantum channel downlinks with adaptive-optics coupling to single-mode fibers

Mark T. Gruneisen
Michael B. Flanagan
Brett A. Sickmiller

SPIE.

Mark T. Gruneisen, Michael B. Flanagan, Brett A. Sickmiller, "Modeling satellite-Earth quantum channel downlinks with adaptive-optics coupling to single-mode fibers," *Opt. Eng.* **56**(12), 126111 (2018), doi: 10.1117/1.OE.56.12.126111.

Modeling satellite-Earth quantum channel downlinks with adaptive-optics coupling to single-mode fibers

Mark T. Gruneisen,[a,*] Michael B. Flanagan,[b] and Brett A. Sickmiller[b]
[a]Air Force Research Laboratory, Directed Energy Directorate, Kirtland AFB, New Mexico, United States
[b]Leidos, Albuquerque, New Mexico, United States

Abstract. The efficient coupling of photons from a free-space quantum channel into a single-mode optical fiber (SMF) has important implications for quantum network concepts involving SMF interfaces to quantum detectors, atomic systems, integrated photonics, and direct coupling to a fiber network. Propagation through atmospheric turbulence, however, leads to wavefront errors that degrade mode matching with SMFs. In a free-space quantum channel, this leads to photon losses in proportion to the severity of the aberration. This is particularly problematic for satellite-Earth quantum channels, where atmospheric turbulence can lead to significant wavefront errors. This report considers propagation from low-Earth orbit to a terrestrial ground station and evaluates the efficiency with which photons couple either through a circular field stop or into an SMF situated in the focal plane of the optical receiver. The effects of atmospheric turbulence on the quantum channel are calculated numerically and quantified through the quantum bit error rate and secure key generation rates in a decoy-state BB84 protocol. Numerical simulations include the statistical nature of Kolmogorov turbulence, sky radiance, and an adaptive-optics system under closed-loop control. [DOI: 10.1117/1.OE.56.12.126111]

Keywords: adaptive optics; quantum communication; quantum networks; quantum key distribution; free-space optical communication; optical fiber.

Paper 171382P received Sep. 1, 2017; accepted for publication Nov. 9, 2017; published online Dec. 27, 2017.

1 Introduction

Propagation of coherent light through atmospheric turbulence leads to wavefront errors that enlarge the classical irradiance and quantum probability distributions at a focus. In a satellite ground station, the size of the photon distribution at the focus increases with the strength of turbulence, which itself varies with the ground-station slew rate, pointing angle, and atmospheric conditions. Recently, we presented results from numerical simulations of quantum channels linking a low-Earth-orbit (LEO) satellite to a terrestrial ground station and showed that a sufficiently high-bandwidth adaptive-optics (AO) system can significantly enhance the performance of daytime quantum channels by increasing photon transmission efficiencies through a field stop (FS) sized for small fields of view (FOVs) to reject daytime sky noise.[1] The results, which were quantified in terms of secure key generation rates in a quantum key distribution (QKD) protocol, are dependent upon the satellite altitude, strength of turbulence, sky radiance, and spatial resolution and correction bandwidth of the AO system.

For applications where single-mode optical fibers (SMFs) are involved, the mode characteristics of the fiber must also be considered. The efficiency of coupling into optical fibers and waveguides can be an important factor for many quantum technologies in a quantum network. Metropolitan networks utilize SMFs for quantum channels.[2,3] Certain concepts for cold-atom interfaces are based on evanescent coupling through optical fiber.[4–6] When integrated with photodiode and nanowire detectors, optical fibers can facilitate the transport of photons and optical coupling to the active detector surface.[7,8] Quantum network components based on integrated photonics are inherently waveguide based.[9] In the case of fiber-coupled single-photon detectors, the mode of the SMF can dictate the detector FOV. Small FOVs, whether achieved with an FS or an SMF, can aid in the filtering of optical noise in a free-space channel. SMFs, however, will introduce additional signal losses when the input field is not matched to the fiber mode.

The effects of atmospheric turbulence on SMF-coupling efficiency have been considered previously for classical optical channels. Dikmelik and Davidson[10] demonstrated numerically that SMF-coupling efficiencies decrease rapidly with increasing link distance and turbulence strength. Ma et al.[11] measured SMF-coupling efficiencies and bit error rates over an 11.8-km free-space optical-communication system using an erbium-doped fiber amplifier and showed favorable agreement with a model based on the statistical nature of turbulence. Laboratory demonstrations showing significant improvement to SMF coupling with AO include an AO system based on an MEMS deformable mirror (DM) with a very large scale integration (VLSI) gradient descent controller and a conventional AO system with a laboratory turbulence simulator.[12,13] Recently, optical communication was demonstrated over a free-space channel linking the International Space Station to a ground station implementing an AO system for the purpose of enhancing SMF-coupling efficiencies.[14] The analysis that follows is, to our knowledge, the first reported numerical analysis that considers and quantifies the benefit of an AO system to a free-space quantum channel where the ground terminal includes SMF-coupled quantum components.[15]

*Address all correspondence to: Mark T. Gruneisen

This report considers a quantum channel downlink between an LEO satellite and a terrestrial ground station implementing an AO system. The quantum channel includes propagation through vacuum, atmospheric turbulence, and atmospheric scattering. The efficiency of coupling from the ground-station primary optic through an FS or into an SMF is treated through numerical simulations. Section 2 describes a terrestrial ground-station configuration with an AO system and a quantum receiver and illustrates the effects of atmospheric turbulence on focal plane irradiance distributions. Section 3 describes the use of fully integrated software to calculate the effects of propagation through turbulence and to simulate the effects of a specified AO system under closed-loop control. Parameters defining the AO system and turbulence conditions are given. Section 4 presents results from the simulations in the form of focal-plane coupling efficiencies as a function of ground-station pointing angle for various turbulence conditions and satellite altitudes. Section 5 presents results in the form of quantum information metrics for varying levels of channel noise associated with sky radiance. Quantum metrics include the quantum bit error rate (QBER) and the rate of secure key bit generation in a decoy-state QKD protocol. Cases with higher-order AO are compared with cases where only wavefront tilt correction (i.e., tracking) is assumed. Results are shown for system configurations that include either a circular FS or an SMF that also serves as the FS. In this comparison, the diameter of the FS is taken to be that of the diffraction-limited Airy disk, and the SMF mode size is optimized for the diffraction-limited case.

The simulations include the effects of elevation-angle-dependent turbulence-induced wavefront errors, high Greenwood frequencies associated with tracking an LEO satellite through turbulence, and the finite bandwidth of a 200-Hz AO system under closed-loop control. Results are presented as mean values calculated from statistically independent realizations of turbulence. Appendix A reviews the analytic solution for power coupling efficiency of a diffraction-limited optical field into an SMF where the SMF mode is approximated by a Gaussian function. This result defines the optimum relationship between the size of the fiber mode and a diffraction-limited focus.

2 Description of a Satellite-Earth Quantum Channel with Ground-Station Adaptive Optics

Figure 1 shows a terrestrial ground-station telescope with components that constitute both an AO system and a quantum receiver. For illustrative purposes, the quantum receiver is shown with components similar to those previously implemented for polarization-based QKD protocols and measurements of Bell-type inequalities.[16–18] In principle, the quantum receiver could be a fiber network, integrated quantum photonics, or any other quantum information-based system.

A beacon wavefront and signal wavefront propagate from a satellite-based source through the Earth's atmosphere to the ground-station primary mirror (PM). For individual photons, the wavefront describes the transverse momentum distribution of the photon. It is assumed that, prior to entering the atmosphere, both wavefronts are free of wavefront errors.

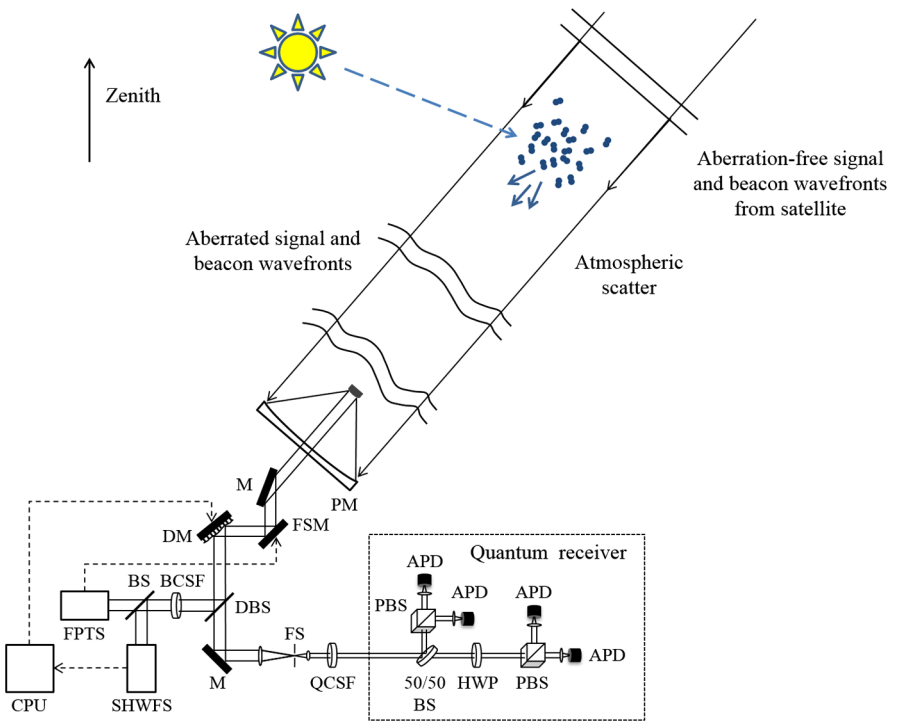

Fig. 1 Schematic of a satellite ground-station with AO and a quantum receiver. Components include a primary mirror (PM), fast steering mirror (FSM), deformable mirror (DM), dichroic beam splitter (DBS), beacon channel spectral filter (BCSF), beam splitter (BS), focal plane tracking sensor (FPTS), Shack–Hartmann wavefront sensor (SHWFS), central processing unit (CPU), mirror (M), field stop (FS), quantum channel spectral filter (QCSF), polarizing beam splitters (PBS), Geiger-mode avalanche photodiodes (APD), and half-wave plate (HWP). Control signals are shown as dashed lines.

The beacon and signal sources emit at slightly different wavelengths to allow chromatic separation at the receiver. A dichroic beam splitter (DBS) directs the beacon wavefronts to wavefront sensors and transmits the signal photons.

A focal plane tracking sensor (FPTS) measures wavefront tilt, and a Shack–Hartmann wavefront sensor (SHWFS) measures higher-order wavefront errors. Control signals generated from these sensors drive a fast steering mirror (FSM) and a DM to compensate for low-order wavefront tilt and higher-order aberrations, respectively. Introducing AO only requires the addition of the FSM and DM as optical elements in the quantum channel. The simulations assume that these components are introduced with negligible loss and effect on polarization. Signal photons transmitted by the DBS propagate to a focus where a system FS defines the quantum channel FOV. A quantum channel spectral filter (QCSF) transmits the signal photons to the quantum receiver while blocking other spectral components. Within the quantum receiver, a 50/50 beam splitter (50/50 BS) randomly directs photons to two mutually unbiased measurement bases. In the reflected path, a polarizing beam splitter (PBS) and two gated avalanche photodiodes (APDs) measure polarization in the rectilinear basis. In the transmitted path, a half-wave plate (HWP) rotates the polarization states by 45 deg for measurement in the diagonal polarization basis. In principle, all or some of the free-space propagation paths shown after the FS could be replaced with SMF.

2.1 *Effects of Turbulence-Induced Aberrations in the Plane of a Field Stop*

Figure 2 shows conceptually the effects of turbulence on the photon wavefront and probability distribution at either an FS or an SMF. A planar optical wavefront propagates through atmospheric turbulence. The resulting aberrated wavefront is incident upon a primary optic and brought to a focus within the system.

Figure 2(a) shows the case where the efficiency of propagation through a circular aperture FS is considered both with and without AO. Optimizing the quantum channel performance requires the FS diameter, d, be adjusted to maximize the transmission of signal photons while minimizing the transmission of noise photons. Maximizing signal photon transmission requires d to be sufficiently large to pass most of the photon probability distribution. Minimizing channel noise, however, requires d to be sufficiently small to block noise photons that are not blocked by spectral and temporal filtering techniques. Figure 2(b) shows the case where the FS is replaced by an SMF. Note that the SMF could be placed in any image plane of the FS. For the case of SMF-coupled quantum detectors, this could be in the focal plane where the APDs are located in Fig. 1.

In this analysis, the classical irradiance distribution is assumed to represent the probability function associated with the transverse momentum of an individual photon. The minimum spot size at the focus occurs in the absence of aberrations. For the case of a planar wavefront with uniform amplitude incident upon a circular aperture, the diffraction-limited irradiance distribution at the focus is described by the Airy function

$$I_{\text{Airy}} = 4\left|\frac{J_1\left(\pi \frac{D_R}{\lambda f} r\right)}{\pi \frac{D_R}{\lambda f} r}\right|^2, \tag{1}$$

with a central disk of diameter $2.44\lambda f/D_R$, where D_R is the diameter of the entrance pupil, λ is the wavelength, and f is the system focal length. Reducing the FS to this diameter passes 84% of the signal while blocking incident light associated with larger field angles. Reducing the FS further decreases both the transmitted sky noise and the signal.[1]

The effect of atmospheric turbulence on the size of the irradiance distribution can be estimated as follows. The strength of turbulence integrated over a propagation path is characterized by Fried's coherence length r_0.[19] Sarazin

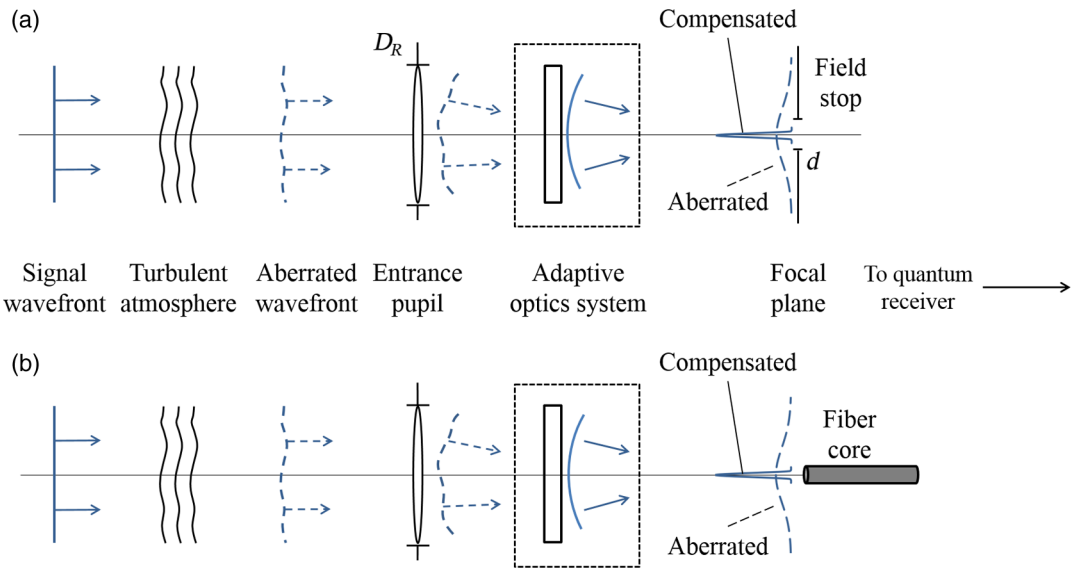

Fig. 2 Block diagram illustrating a planar wavefront propagating through atmospheric turbulence, incident upon a primary optic of diameter D_R, and brought to a focus at either (a) a circular aperture of diameter d or (b) the entrance of an SMF. An AO system is included to compensate for turbulence-induced wavefront errors.

and Roddier[20,21] computed the angular full width at half maximum of the long-exposure irradiance distribution with turbulence to be approximately λ/r_0. In analogy to the Airy disk, we define the turbulence-induced spot size to be that which captures about 84% of the power. For primary optic diameters larger than r_0, this aberrated spot size at the focus is found to be $\sim 2\lambda f/r_0$. High signal transmission efficiency requires the diameter of the FS to be increased by a factor of $D_R/1.22r_0$ relative to the diffraction-limited case. In a noisy channel, this increases the transmitted noise photons by a factor of $(D_R/1.22r_0)^2$.

Atmospheric turbulence is characterized by standard altitude-dependent turbulence profiles. The strength of turbulence is both angle and wavelength dependent. For the commonly used $HV_{5/7}$ turbulence profile,[22] henceforth referred to as $1xHV_{5/7}$, and a wavelength of 780 nm, r_0 ranges from about 9 to 4 cm for pointing angles ranging from 0 deg to 75 deg from zenith, respectively. For a $D_R =$ 1 m diameter receiver aperture, turbulence will increase the size of the signal distribution by a factor of about 9 to 20, respectively. This blurring of the signal distribution requires the FS to be significantly larger than the Airy disk to avoid signal losses and, in this example with moderate turbulence, can increase noise by factors ranging from about 80 to 400.

2.2 *Optical Fiber Coupling Efficiency*

In the case where the FS is replaced by the SMF, the fiber mode characteristics must also be considered. The efficiency with which an optical field, F_{optical}, couples into the mode, F_{01}, of an SMF is given by the normalized projection of the optical field onto the fiber mode

$$\rho = \left| \frac{|\langle F_{\text{optical}} | F_{01} \rangle|}{\|F_{\text{optical}}\| \|F_{01}\|} \right|^2. \tag{2}$$

In the simulations that follow, the fiber mode is assumed to be Gaussian with radius ω_0. For an aperture of dimension D and focal length f, the efficiency of mode matching is characterized by the parameter $\beta = \pi D\omega_0/2f\lambda$. The central obscuration of the telescope receiver is assumed to be 20%, and the fiber mode radius is assumed to satisfy $\beta = 1.07$. This value for β yields optimum coupling efficiency for a diffraction-limited field in accordance with the analysis of Ruilier, reproduced in Appendix A.

3 Numerical Simulations of a Satellite-Earth Channel

This section introduces the atmospheric and AO parameters assumed in the simulations and describes the use of fully integrated software to model the effects of wave propagation through the atmosphere, the effects of an AO system under closed-loop control, the efficiency of transmission through a circular FS, and the efficiency of coupling into an SMF.

3.1 *Numerical Methods for Calculating the Effects of Atmospheric Turbulence and an Adaptive-Optics System under Closed-Loop Control*

In principle, an AO system can restore an aberrated wavefront to near-diffraction-limited quality. In practice, however, AO does not completely compensate for turbulence-induced aberrations. Limitations occur due to the finite spatial resolution and finite temporal response of the AO system. For a given set of atmospheric parameters and AO system specifications, the performance of an optical channel can be evaluated using numerical methods.

Numerical simulations are performed with the Atmospheric Compensation Simulation (ACS) code developed by Leidos.[23,24] ACS has been anchored to experiment and used to anchor other simulation codes.[25] The software generates statistical realizations of atmospheric turbulence in the form of two-dimensional phase functions as shown in Fig. 3. Each phase screen is a random realization of turbulence consistent with Kolmogorov statistics and the specified turbulence strength profile. Numerical methods based on scalar Fresnel integrals[26,27] propagate the optical field from the transmitter through the phase screens[28] to the receiving aperture. Simulations are performed for receiver pointing angles ranging from zenith to 75 deg from zenith. For each elevation angle, 10 realizations of atmospheric turbulence are simulated. For each realization of turbulence, the atmosphere is simulated by 10 phase screens distributed throughout the atmospheric path. The simulated AO system includes an FPTS and FSM for tilt estimation and correction and an SHWFS and DM for higher-order aberration correction. These components are simulated in a closed loop for iterative feedback control. The ACS hardware emulations include models for the wavefront sensor cameras that include real-world effects, such as noise, pixel diffusion, and latencies. The simulations reported here assume one frame of latency and a very high signal-to-noise ratio but omit pixel diffusion. The complex optical field resulting from propagation through turbulence and an AO system is then used to calculate the transmission efficiency through a circular FS or into an SMF. In the latter case, the transmission efficiency is calculated via the normalized projection of the optical field onto the fiber mode.

3.2 *Adaptive-Optics System Parameters*

Table 1 summarizes the AO system parameters assumed in the simulations. The FPTS is modeled as a lens and focal plane quadrant detector. The SHWFS is modeled as a 16×16 element array of lenslets and quadrant detectors. The SHWFS is assumed to be shot-noise limited as is typically the case for systems with cooperative beacons. The DM is modeled as a continuous face sheet driven by a 19×19 array of actuators comprised of a 17×17 array of active actuators with an additional ring of slaved actuators. In the simulations, the FPTS centroid, SHWFS centroids, and residual wavefront errors are updated at 2 kHz. The FSM and DM are also updated at 2 kHz. The tracking bandwidth is 150 Hz, and the bandwidth for higher-order correction is 200 Hz. These system parameters are considered to be within the state of the art.

It is assumed that the cooperative beacon on the satellite provides light at 810-nm wavelength for the FPTS and SHWFS. The signal wavelength is assumed to be 780 nm allowing separation of the two wavelengths. Applying wavefront correction at a wavelength that is shorter than the beacon wavelength can lead to residual wavefront errors. While these errors are accounted for in the simulations, they are negligible due to the small separation in wavelengths. Similarly, the beacon and quantum channel pulses

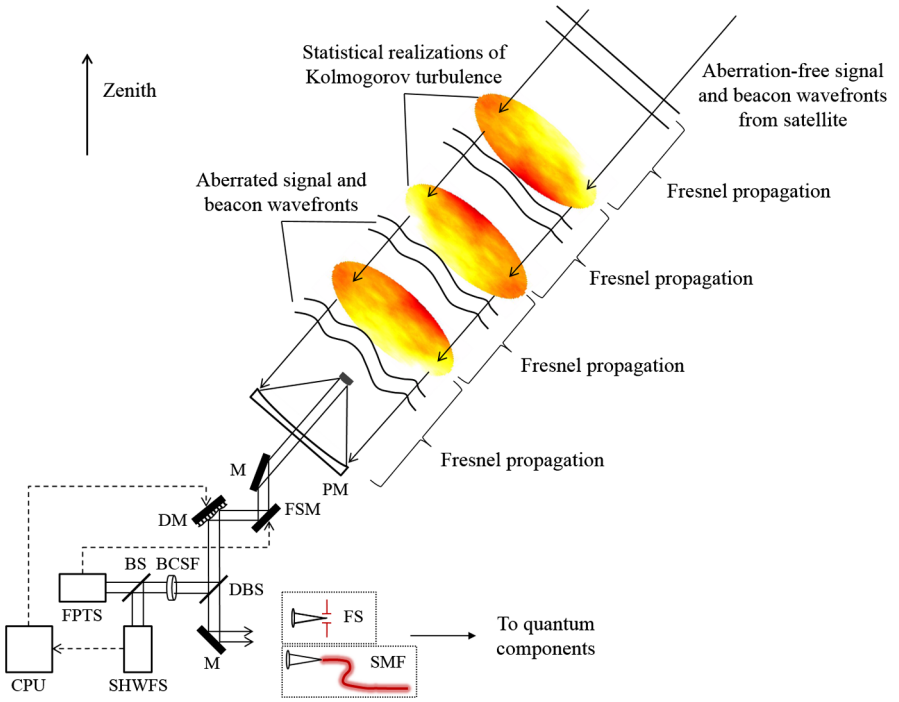

Fig. 3 Schematic of a ground-station quantum receiver illustrating elements of the numerical simulations, including wave propagation through statistical realizations of turbulence, a closed-loop AO system, and transmission either through an FS or into an SMF.

Table 1 AO system parameters assumed in the simulations.

AO parameters		
Beacon wavelength	810	nm
Signal wavelength	780	nm
SHWFS lenslet array size	16×16	—
DM actuator array size	19×19	—
Wavefront sensor update rate	2	kHz
FSM and DM update rate	2	kHz
Tracking bandwidth	150	Hz
Higher-order correction bandwidth	200	Hz

are separated in time but on a timescale over which the atmosphere is static in the simulations.

3.3 *Atmospheric Turbulence Parameters*

The effects of turbulence on an optical field are characterized by temporal, angular, and spatial coherence parameters. The temporal coherence, given by the Greenwood frequency f_G, depends on the telescope slew rate and, therefore, the altitude of the satellite. The angular coherence is given by the isoplanatic angle θ_0. The spatial coherence is given by Fried's coherence length r_0. Residual wavefront errors will occur when Greenwood frequencies exceed the AO correction bandwidth, isoplanatic angles become smaller than the angular subtense of the source, or r_0 becomes smaller than the SHWFS subaperture size, d_l. Rytov is a direct measure of scintillation experienced by the optical field at the receiver entrance pupil. Rytov values greater than about 0.4 indicate deep turbulence where scintillation degrades the performance of the AO system. In the presence of scintillation, the SHWFS is unable to accurately measure wavefront errors due to intensity nulls in the field.

For the purpose of analysis, it is assumed that the satellite travels in either a 400- or 800-km-altitude circular orbit. The telescope slews to follow the motion of the satellite. The altitude-dependent wind speed is described by the Bufton wind profile. To consider the worst-case scenario, the wind direction is assumed to be opposite the slew direction producing the highest Greenwood frequency for a particular turbulence profile.

Table 2 shows turbulence parameters calculated at 780-nm wavelength for five elevation angles, three turbulence profiles, and two orbit altitudes. The three turbulence profiles, designated as $1\text{xHV}_{5/7}$, $2\text{xHV}_{5/7}$, and $3\text{xHV}_{5/7}$, are based on the $\text{HV}_{5/7}$ model with the altitude-dependent structure constant, C_n^2, values multiplied by a scaling factor of 1, 2, or 3. The AO system characteristics assumed in this analysis are less than ideal for complete compensation of turbulence-induced wavefront errors in an LEO-Earth channel. Partial compensation, however, can still provide a benefit, and such a system may be of interest based on cost and availability. For cases where the turbulence characteristics exceed the design specifications of the AO system assumed in the analysis, values are shown in bold.

For a 10-cm transmitter aperture, the angular subtense of the source lies within the isoplanatic angles for all cases. For the 400-km orbit, Greenwood frequencies exceed the 200-Hz AO system bandwidth for all cases shown. For the 800-km orbit, lower slew rates result in lower Greenwood

frequencies and, within 45 deg of zenith in $1xHV_{5/7}$ turbulence, f_G lies within the AO system bandwidth. At the 75-deg elevation angle, Rytov values indicate deep turbulence conditions. For $D_R = 1$ m, the SHWFS subaperture size in pupil space is $d_l = 6.25$ cm. In $3xHV_{5/7}$ turbulence, r_0 is smaller than the subaperture size for all angles considered. This leads to underresolved local wavefront tilts and reduced AO performance.[28,29] In $1xHV_{5/7}$ turbulence, wavefront tilts are well resolved within 45 deg of zenith.

4 Optical Efficiencies with Turbulence-Induced Wavefront Errors and Adaptive-Optics Compensation

Simulations are performed in angle space in the pupil plane assuming a $D_T = 10$ cm transmitter optic and a $D_R = 1$ m PM with a 20% obscuration. The diameter of the FS is defined by a 2-μrad diffraction-limited FOV. The mode diameter of the SMF is given by $\beta = 1.07$. FS and SMF-coupling efficiencies are calculated for the field-angle-dependent turbulence parameters given in Table 2. Results from the simulations are summarized in Fig. 4 as a function of zenith angle for three strengths of turbulence and two satellite orbit altitudes. Efficiencies are shown as mean values representing an average over 10 statistically independent realizations of turbulence. Each realization consists of a 500-frame closed-loop statistically correlated time series. The mean values are normalized to the efficiencies that would be achieved with a perfect diffraction-limited wavefront passing through a circular FS whose diameter is matched to the central lobe of the Airy function. For this choice of normalization, a maximum value of unity corresponds to an aberration-free wavefront passing through a circular FS with about 84% efficiency.

Results calculated with tracking but without the benefit of higher-order AO are shown as dashed lines. Those calculated with higher-order AO are shown as solid lines. FS transmission efficiencies are shown as open circles. SMF-coupling efficiencies are shown as solid circles. Without the benefit of AO, efficiencies are generally low as a consequence of turbulence-induced wavefront errors. SMF-coupling efficiencies are consistently lower than FS transmission efficiencies due to the increased losses associated with coupling into the fiber mode. Efficiencies are highest at zenith where the atmospheric path is shortest and decrease with increasing zenith angle and associated increased atmospheric path length and wavefront errors.

Figure 4(a) shows results for the case of $1xHV_{5/7}$ turbulence and a 400-km-altitude circular satellite orbit. With

Table 2 Atmospheric turbulence parameters at 780-nm wavelength for five elevation angles for 400- and 800-km-altitude circular orbits. Parameters include Fried's coherence length r_0, the isoplanatic angle θ_0, Rytov, and the Greenwood frequency f_G calculated for $1xHV_{5/7}$, $2xHV_{5/7}$, and $3xHV_{5/7}$ turbulence profiles.

	400-km altitude				800-km altitude			
Zenith angle (deg)	r_0 (cm)	θ_0 (μrad)	Rytov	f_G (Hz)	r_0 (cm)	θ_0 (μrad)	Rytov	f_G (Hz)
				$1xHV_{5/7}$				
0	8.5	11.82	0.04	**250**	8.5	11.82	0.04	143
30	7.8	9.47	0.05	**275**	7.8	9.44	0.05	158
45	6.9	6.86	0.06	**315**	6.9	6.83	0.07	182
60	**5.6**	3.96	0.12	**403**	**5.6**	3.94	0.12	**239**
75	**3.8**	1.41	0.40	**697**	**3.8**	1.40	**0.40**	**436**
				$2xHV_{5/7}$				
0	**5.6**	7.8	0.07	**380**	**5.6**	7.80	0.07	**217**
30	**5.2**	6.25	0.09	**416**	**5.1**	6.23	0.09	**239**
45	**4.6**	4.53	0.13	**477**	**4.6**	4.51	0.13	**277**
60	**3.7**	2.61	0.24	**611**	**3.7**	2.60	0.25	**362**
75	**2.5**	0.93	0.79	**1056**	**2.5**	0.93	**0.81**	**661**
				$3xHV_{5/7}$				
0	**4.4**	6.11	0.10	**485**	**4.4**	6.11	0.10	**277**
30	**4.0**	4.90	0.13	**531**	**4.0**	4.88	0.14	**305**
45	**3.6**	3.55	0.19	**609**	**3.6**	3.53	0.20	**353**
60	**2.9**	2.05	0.36	**780**	**2.9**	2.04	0.37	**462**
75	**2.0**	0.73	1.19	**1347**	**2.0**	0.73	**2.21**	**843**

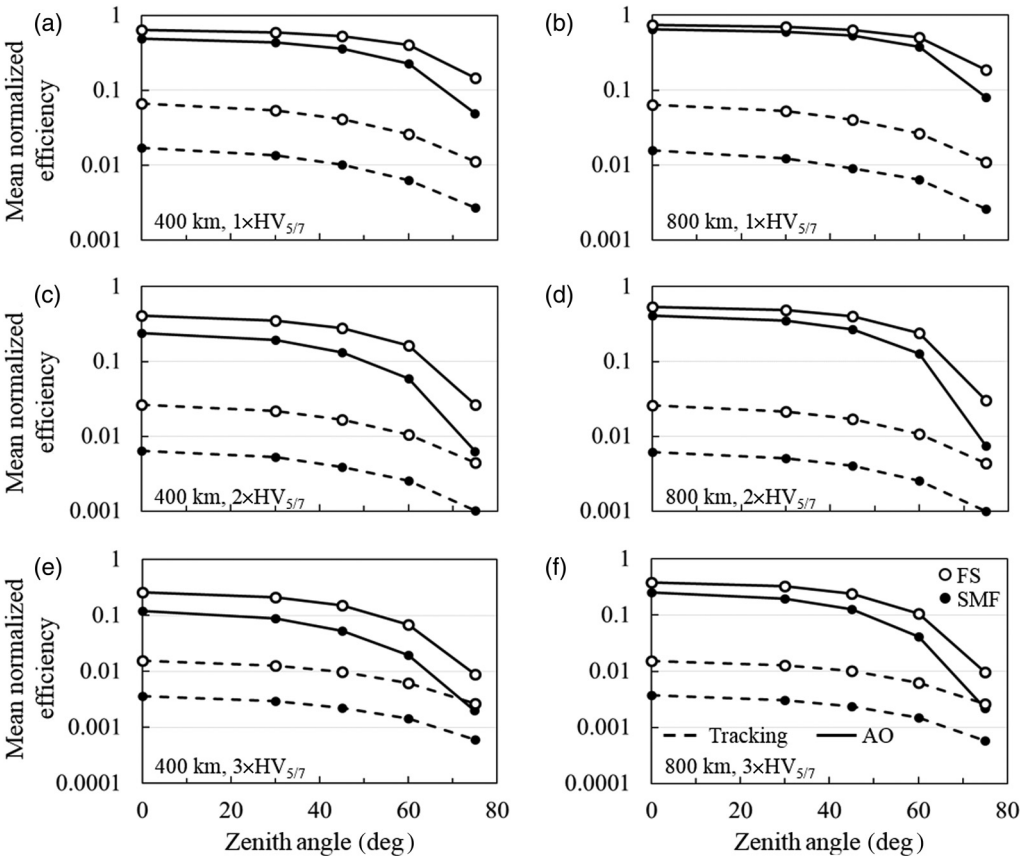

Fig. 4 Mean normalized efficiencies versus ground-station pointing angle associated with transmission through a circular FS, shown as open circles, and coupling into an SMF, shown as solid circles. Results calculated with tracking only are shown as dashed lines. Those calculated with higher-order AO are shown as solid lines. Combinations of turbulence strength and circular orbit altitude are given by (a) $1xHV_{5/7}$ and 400 km, (b) $1xHV_{5/7}$ and 800 km, (c) $2xHV_{5/7}$ and 400 km, (d) $2xHV_{5/7}$ and 800 km, (e) $3xHV_{5/7}$ and 400 km, and (f) $3xHV_{5/7}$ and 800 km.

tracking only, FS transmission efficiencies for ground-station pointing angles of 0 deg, 30 deg, and 60 deg from zenith are about 7%, 5%, and 3%, respectively. SMF-coupling efficiencies are about a factor-of-four lower at 2%, 1%, and 0.6%, respectively. With the addition of higher-order AO, FS transmission efficiencies increase to 64%, 60%, and 40% and SMF-coupling efficiencies increase to 49%, 44%, and 23% at the respective pointing angles. These correspond to an order-of-magnitude improvement in FS transmission and a factor-of-30 improvement in SMF-coupling efficiency. For SMF-coupled detectors, higher-order AO would lead to a corresponding increase in photon detection probability. For this case, Greenwood frequencies range from 250 to 697 Hz exceeding the 200-Hz closed-loop bandwidth at all angles. AO leads to significant improvements in efficiencies, but wavefront compensation is imperfect and peak efficiencies do not approach unity.

Figure 4(b) shows the corresponding results for an 800-km-altitude orbit. Results calculated with tracking are nearly identical to the 400-km orbit case owing to the fact that wavefront errors due to turbulence near the receiver are not affected by propagation prior to encountering the turbulence. With higher-order AO, FS transmission efficiencies increase to 74%, 70%, and 51% and SMF-coupling efficiencies increase to 65%, 61%, and 38% at the respective pointing angles of 0 deg, 30 deg, and 60 deg from zenith. Efficiencies calculated with AO are higher than those for the 400-km orbit as a consequence of the reduced satellite angular velocity, lower slew rates, and corresponding Greenwood frequencies. Within 45 deg, where turbulence parameters fall within the correction bandwidth and spatial resolution of the AO system, efficiencies remain above about 50%. At lower elevation angles, increased turbulence begins to challenge the performance of the AO system and efficiencies decline.

Figures 4(c) and 4(d) show the corresponding results for $2xHV_{5/7}$ turbulence, and Figs. 4(e) and 4(f) show results for $3xHV_{5/7}$ turbulence. Relative to the results of Figs. 4(a) and 4(b), stronger turbulence leads to increased residual wavefront errors and reduced coupling efficiencies. With increased Greenwood frequencies and underresolved subaperture wavefront tilts, the AO system can only partially correct wavefront errors relative to the theoretical diffraction limit. In this regime, efficiencies are improved significantly relative to the tracking case but reduced relative to the $1xHV_{5/7}$ turbulence case. With $3xHV_{5/7}$ turbulence, the peak SMF efficiencies with tracking are only about 0.4%, 0.3%, and 0.1% at 0 deg, 30 deg, and 60 deg from zenith, respectively. In this case of strong turbulence, higher-order AO increases SMF efficiencies to 12%, 9%, and 2% for the 400-km orbit and 25%, 20%, and 4% for the 800-km orbit at the respective angles.

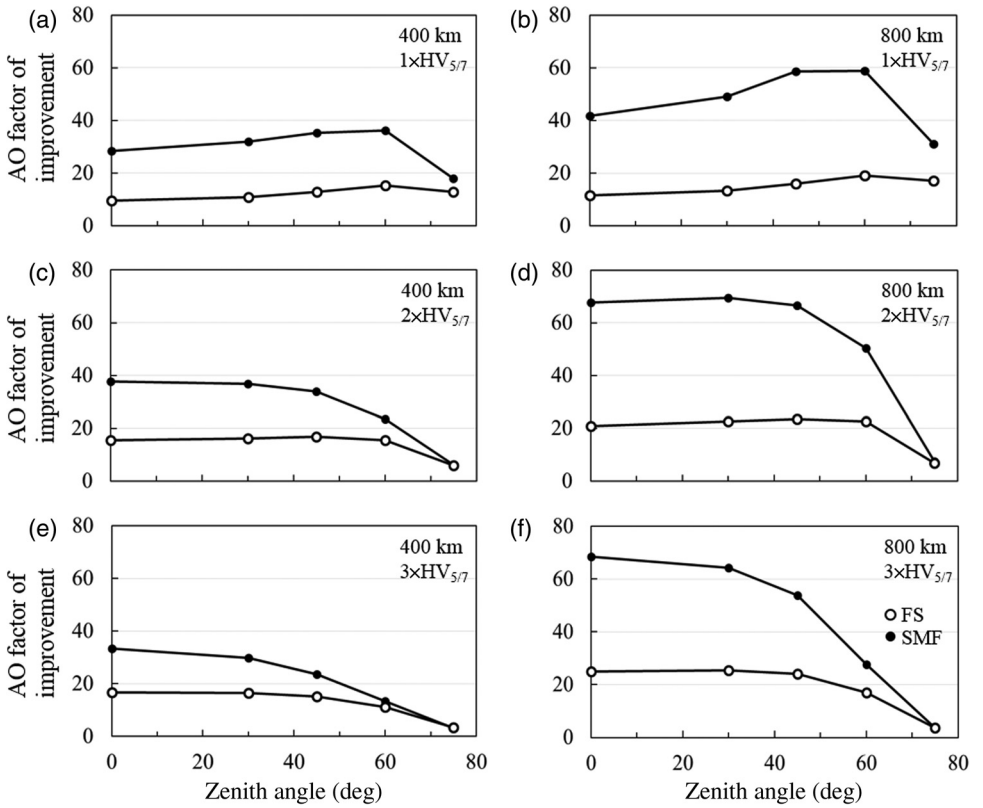

Fig. 5 Factors of improvement in optical efficiencies resulting from implementation of a 200-Hz-bandwidth AO system. Results are shown for the case of transmission through a circular FS, as open circles, and coupling into a single-mode optical fiber, as solid circles. Combinations of turbulence strength and circular orbit altitude are given by (a) 1xHV$_{5/7}$ and 400 km, (b) 1xHV$_{5/7}$ and 800 km, (c) 2xHV$_{5/7}$ and 400 km, (d) 2xHV$_{5/7}$ and 800 km, (e) 3xHV$_{5/7}$ and 400 km, and (f) 3xHV$_{5/7}$ and 800 km.

Figure 5 shows the factors of improvement provided by the simulated AO system in correspondence to the cases shown in Fig. 4. Factors of improvement to FS transmission efficiency are shown as open circles and those for SMF-coupling efficiency are shown as solid circles. AO can enhance SMF-coupling efficiency by nearly 70-fold. Factors of improvement are higher for SMF coupling compared with those for FS transmission owing to the fact that SMF-coupling efficiencies are more adversely affected by turbulence than simple transmission through an aperture where mode-matching constraints do not apply.

5 Quantum Channel Performance with Tracking and Higher-Order Adaptive Optics

The degree to which the quantum channel will benefit from AO depends on the application and conditions in the free-space channel. The performance of the channel can be quantified through metrics from quantum information theory. This section considers the QBER as defined in QKD as a metric for channel performance. Simulations are performed for varying ground-station pointing angles, atmospheric conditions, and two satellite altitudes.

5.1 *Quantum Bit Error Rates*

For applications based on the detection of polarization states of individual photons, such as discrete-variable QKD or measurements of Bell inequalities, quantum bit errors will occur due to noise in the channel resulting from background photons, detector dark counts, and cross talk in polarization measurements. The overall QBER associated with signal photons in a QKD protocol can be written as[30]

$$E_\mu = \frac{e_0 Y_0 + e_{\text{detector}}(1 - e^{-\eta\mu})}{Y_0 + 1 - e^{-\eta\mu}}, \tag{3}$$

where e_0 is the error rate due to noise and e_{detector} is the probability that an incorrect bit value occurred due to polarization cross talk. The background detection probability, including contributions from sky radiance and detector dark counts, is calculated.

$$Y_0 = N_b \eta_{\text{receiver}} \eta_{\text{spectral}} \eta_{\text{detector}} + 4 f_{\text{dark}} \Delta t, \tag{4}$$

where $N_b \eta_{\text{receiver}} \eta_{\text{spectral}} \eta_{\text{detector}}$ is the probability of detecting a sky-noise photon, η_{spectral} is the efficiency of transmission through the spectral filter, η_{detector} is the efficiency of photon detection, and η_{receiver} is the efficiency of transmission through the remaining receiver optics. The probability of a detection event occurring due to detector noise within a time interval Δt is $4 f_{\text{dark}} \Delta t$, where f_{dark} is the detector dark count rate at each of four identical detectors. The total signal transmission efficiency η also includes

angle-dependent terms associated with propagation from the transmitter aperture through free space, including the atmospheric path

$$\eta = \eta_{\text{geo}}\eta_{\text{trans}}\eta_{\text{spatial}}\eta_{\text{receiver}}\eta_{\text{spectral}}\eta_{\text{detector}}, \tag{5}$$

where η_{geo} is the angle-dependent geometrical coupling efficiency between the transmitter and receiver apertures due to diffraction and finite aperture sizes and η_{trans} is the angle-dependent transmission efficiency associated with atmospheric scattering and absorption. The photon capture efficiency associated with atmospheric turbulence, η_{spatial}, is defined to include the turbulence-related losses associated with both transmitter-to-receiver aperture coupling and propagation through the FS of the receiver or into an SMF.

The number of sky-noise photons, N_b, entering the receiver in a detection window is proportional to the sky radiance according to the radiometric expression[31]

$$N_b = \frac{H_b \Omega_{\text{FOV}} \pi R^2 \lambda \Delta\lambda \Delta t}{hc}, \tag{6}$$

where H_b is the sky radiance in $\text{W}/(\text{m}^2\,\text{sr}\,\mu\text{m})$, Ω_{FOV} is the receiver solid-angle FOV, R is the radial extent of the primary optic, λ is the optical wavelength, $\Delta\lambda$ is the spectral filter bandpass in μm, Δt is the integration time for photon counting, h is Planck's constant, and c is the speed of light. The solid-angle FOV is related to the linear-angle FOV $\Delta\theta$ by $\Omega_{\text{FOV}} = \pi\Delta\theta^2/4$. For cases that assume a circular FS, the linear-angle FOV is assumed to be the diffraction-limited FOV, $\Delta\theta_D = 2.44\lambda/D$. For cases that assume an SMF, the numerical aperture of the fiber results in an effective FOV that is approximately ½ the diffraction-limited FOV. While mode matching with the fiber introduces signal losses, the smaller FOV created by the fiber mode can reduce sky noise by approximately a factor of 4 compared with the FS.

5.2 *Satellite-to-Earth Quantum Channel Parameters*

QBERs are calculated for the AO parameters given in Table 1, the atmospheric turbulence parameters given in Table 2, and the remaining channel parameters given in Table 3. For the purpose of this example, the quantum source is assumed to emit a weak coherent pulse with a mean photon number of $\mu = 0.45$, a value determined to be optimum for the decoy-state QKD protocol.[32] Background sky radiance levels considered include a nighttime value of $H_b = 1.5 \times 10^{-2}$ $\text{W}/(\text{m}^2\,\text{sr}\,\mu\text{m})$ and daytime values of 25 and 100 $\text{W}/(\text{m}^2\,\text{sr}\,\mu\text{m})$.[31,32] The detector dark count rate is 250 Hz. Polarization cross talk is taken to be $e_{\text{detector}} = 2.8\%$, an experimentally measured value in a satellite-Earth optical link.[33] Spatial filtering of sky noise is included via a $\Delta\theta = 2$ μrad receiver FOV for the case with an FS and a $\Delta\theta = 1$ μrad FOV for the case with an SMF. This latter value was determined to yield the optimum SMF-coupling efficiency in the absence of aberrations. Spectral and temporal filtering are included via a $\Delta\lambda = 0.2$ nm spectral filter bandpass and a $\Delta t = 1$ ns detector gate duration.

Parameters contributing to optical efficiency include the transmitter and receiver aperture diameters, $D_T = 10$ cm and $D_R = 1$ m, respectively. The angle-dependent aperture-to-aperture coupling efficiency η_{geo} is approximated by the Friis equation, $\eta_{\text{geo}} = (\pi D_T D_R/4\lambda z)^2$, which assumes

Table 3 Quantum channel parameters assumed in the simulations.

Quantum channel parameters			
Quantity	Symbol	Value	Units
	Source parameters		
Quantum channel wavelength	λ	780	nm
Mean photon number	μ	0.45	—
Decoy-state mean photon number	ν	0.05	—
	Noise sources		
Sky radiance	H_b	0.015, 25, and 100	$\text{W}/(\text{m}^2\,\text{sr}\,\mu\text{m})$
Detector dark count rate	f_{dark}	250	Hz
Polarization cross talk	e_{detector}	0.028	—
	Optical noise filtering parameters		
Receiver FOV with circular FS	$\Delta\theta$	2	μrad
Receiver FOV with SMF	$\Delta\theta$	1	μrad
Spectral filter bandpass	$\Delta\lambda$	0.2	nm
Detector gate duration	Δt	1	ns

Table 3 (*Continued*).

Quantum channel parameters			
Quantity	Symbol	Value	Units
		Optical efficiency parameters	
Propagation distance, 400-km alt. orbit	z	400 to 1175	km
Propagation distance, 800-km alt. orbit	z	800 to 2033	km
Transmitter aperture diameter	D_T	10	cm
Receiver aperture diameter	D_R	100	cm
Aperture-to-aperture (geometrical) coupling efficiency, 400-km alt. orbit	η_{geo}	6.3×10^{-2} at 0-deg zenith to 7.3×10^{-3} at 75-deg zenith	—
Aperture-to-aperture (geometrical) coupling efficiency, 800-km alt. orbit	η_{geo}	1.6×10^{-2} at 0-deg zenith to 2.5×10^{-3} at 75-deg zenith	—
Atmospheric transmission, winter	η_{trans}	0.96 at 0-deg zenith to 0.87 at 75-deg zenith	—
Atmospheric transmission, summer	η_{trans}	0.92 at 0-deg zenith to 0.74 at 75-deg zenith	—
Turbulence-related transmission	η_{spatial}	Calculated in simulation	—
Receiver transmission	η_{rec}	0.5	—
Spectral filter transmission	η_{filt}	0.9	—
Detector efficiency	η_{det}	0.6	—

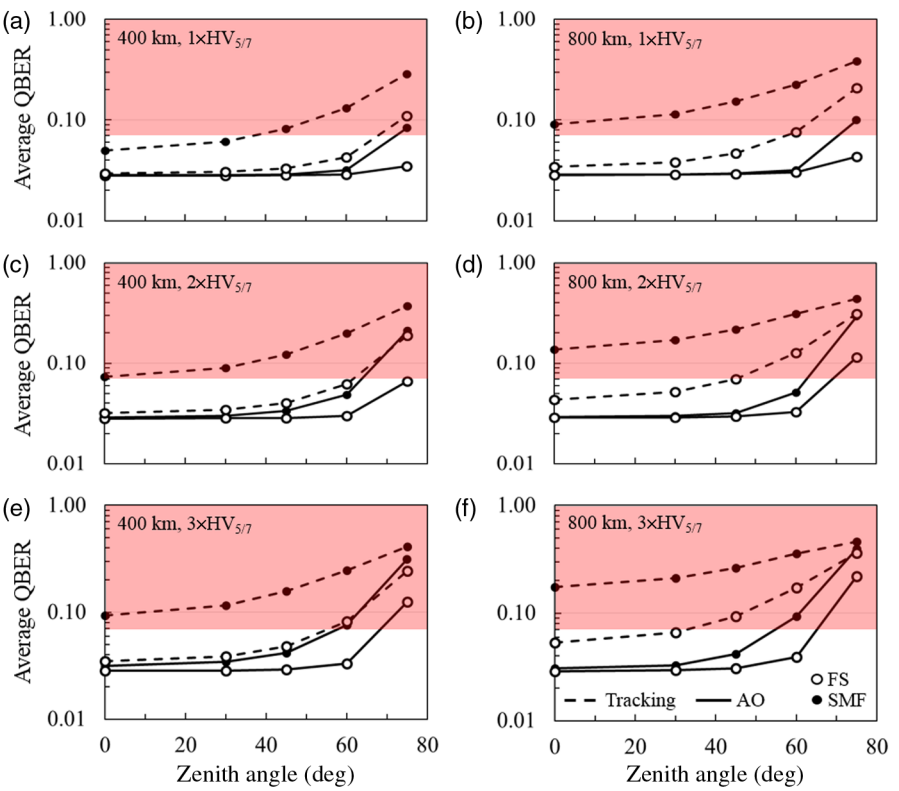

Fig. 6 Average QBERs versus ground-station pointing angle calculated assuming a nighttime sky radiance of $H_b = 1.5 \times 10^{-2}$ W/(m^2 sr μm) and either a circular FS, shown as open circles, or an SMF, shown as solid circles. Results calculated with tracking only are shown as dashed lines. Those calculated with higher-order AO are shown as solid lines. Combinations of turbulence strength and circular orbit altitude are given by (a) 1xHV$_{5/7}$ and 400 km, (b) 1xHV$_{5/7}$ and 800 km, (c) 2xHV$_{5/7}$ and 400 km, (d) 2xHV$_{5/7}$ and 800 km, (e) 3xHV$_{5/7}$ and 400 km, and (f) 3xHV$_{5/7}$ and 800 km.

a uniformly illuminated transmitter aperture.[34,35] The propagation distance z is calculated for 400- and 800-km satellite orbit altitudes with elevation angles ranging from zenith to 75 deg from zenith. The angle-dependent transmission efficiencies η_{trans} are calculated with MODTRAN assuming clear sky conditions. Assumed values range from $\eta_{\text{trans}} = 0.92$ at zenith to $\eta_{\text{trans}} = 0.74$ at 75 deg from zenith. Efficiencies associated with turbulence-related losses, η_{spatial}, are calculated in the simulation. In the absence of turbulence-related losses, $\eta_{\text{spatial}} = 1$ and the signal transmission efficiencies η, expressed in dB of loss, are ~18 to 28 dB for the 400-km orbit and 24 to 33 dB for the 800-km orbit. The spectral filter transmission is $\eta_{\text{spectral}} = 0.9$ and the detector efficiency is $\eta_{\text{detector}} = 0.6$. The collective optical efficiency of the remaining components in the receiver is $\eta_{\text{receiver}} = 0.5$.

Strengths of turbulence include $1\text{xHV}_{5/7}$, $2\text{xHV}_{5/7}$, and $3\text{xHV}_{5/7}$. Cloud-free sky conditions are assumed, and the error rate due to noise, e_0, taken to be ½ under the simplifying assumption of the background is random.

5.3 *Quantum Bit Error Rate Simulation Results*

Numerical results for the QBER, E_μ, are calculated from Eq. (3) for each turbulence frame. The average values over all frames across the 10 realizations of turbulence are summarized in Figs. 6–8 as a function of the ground-station pointing angle. QBER values are calculated for 400- and 800-km satellite altitudes and $1\text{xHV}_{5/7}$, $2\text{xHV}_{5/7}$, and $3\text{xHV}_{5/7}$ atmospheric turbulence profiles and are displayed in correspondence to the fiber coupling efficiencies shown in Fig. 4. The maximum acceptable value for the QBER will depend on the requirements for a given quantum communication application. Previously, the QBER was considered a threshold metric for the decoy-state QKD protocol with a satellite-Earth quantum channel.[32] QBERs >7% precluded secure key generation. In Figs. 6–8, regions of 7% and higher are shaded in red for illustrative purposes. Because the plotted QBERs represent averages, some frames within the time series will deviate from the average values. In some cases where the average QBER is >7%, there will be atmospheric frames where the QBER falls sufficiently below 7% to produce nonzero secure key rates.

Figure 6 shows results calculated assuming a nighttime sky radiance value of $H_b = 1.5 \times 10^{-2}$ W/(m^2 sr μm). For the case of the SMF, shown as solid circles, QBERs are generally large with tracking only. However, with AO, QBERs remain below 3% for pointing angles within 50 deg of zenith even for the case of strong turbulence. For the case of the FS, shown as open circles, the larger FOV permits low QBERs with tracking only. It should be noted that in the relatively benign nighttime sky-noise scenario, small diffraction-limited FOVs are not necessarily required for spatial filtering of sky noise.

Figure 7 shows results calculated assuming a daytime sky radiance value of $H_b = 25$ W/(m^2 sr μm). This value

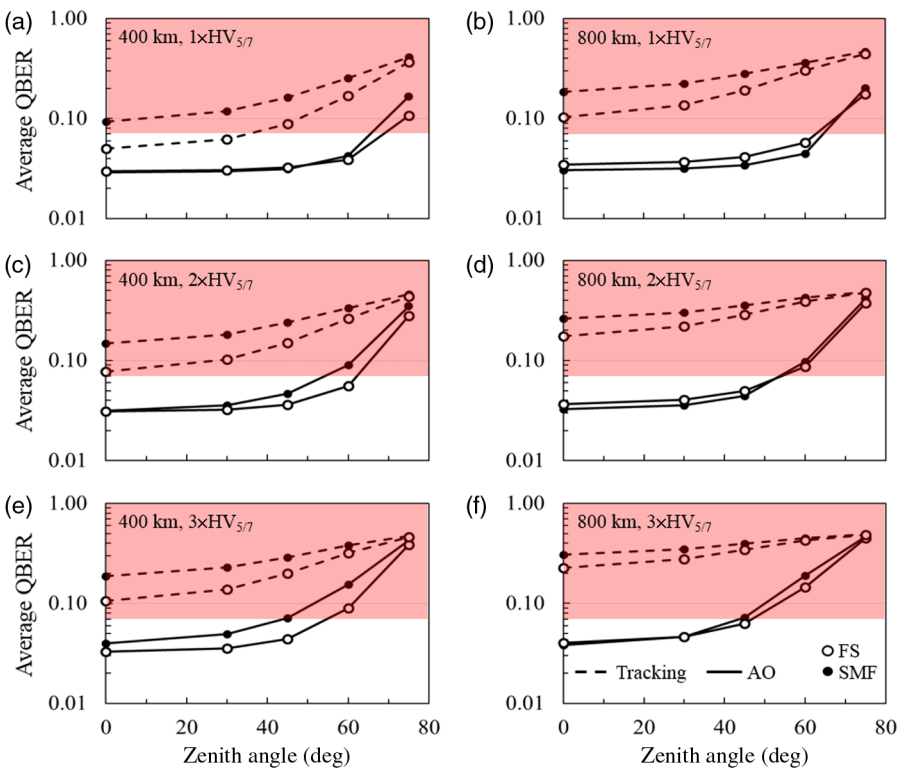

Fig. 7 Average QBERs versus ground-station pointing angle calculated assuming a daytime sky radiance of $H_b = 25$ W/(m^2 sr μm) and either a circular FS, shown as open circles, or an SMF, shown as solid circles. Results calculated with tracking only are shown as dashed lines. Those calculated with higher-order AO are shown as solid lines. Combinations of turbulence strength and circular orbit altitude are given by (a) $1\text{xHV}_{5/7}$ and 400 km, (b) $1\text{xHV}_{5/7}$ and 800 km, (c) $2\text{xHV}_{5/7}$ and 400 km, (d) $2\text{xHV}_{5/7}$ and 800 km, (e) $3\text{xHV}_{5/7}$ and 400 km, and (f) $3\text{xHV}_{5/7}$ and 800 km.

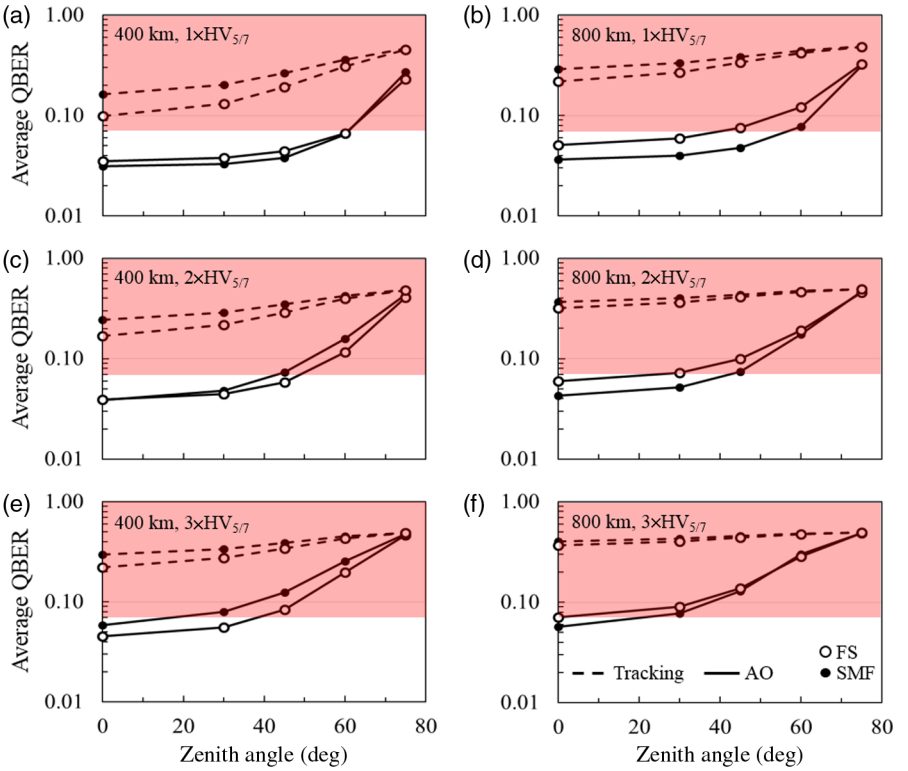

Fig. 8 Average QBERs versus ground-station pointing angle calculated assuming a daytime sky radiance of $H_b = 100$ W/(m^2 sr μm) and either a circular FS, shown as open circles, or an SMF, shown as solid circles. Results calculated with tracking only are shown as dashed lines. Those calculated with higher-order AO are shown as solid lines. Combinations of turbulence strength and circular orbit altitude are given by (a) 1xHV$_{5/7}$ and 400 km, (b) 1xHV$_{5/7}$ and 800 km, (c) 2xHV$_{5/7}$ and 400 km, (d) 2xHV$_{5/7}$ and 800 km, (e) 3xHV$_{5/7}$ and 400 km, and (f) 3xHV$_{5/7}$ and 800 km.

for the background radiance is more than 3 orders of magnitude larger than the nighttime scenario summarized in the preceding figure. The small field angles assumed for both the FS and the SMF provide a substantial level of noise filtering but can also introduce substantial signal losses as a consequence of atmospheric turbulence. With the spectral and temporal filtering conditions assumed, QBERs calculated with tracking only are unacceptably large for nearly all cases shown. With AO however, QBERs remain in relatively benign territory for a range of ground-station pointing angles. Under moderate 1xHV$_{5/7}$ turbulence conditions, QBERs <7% occur within 60 deg of zenith. Under strong 3xHV$_{5/7}$ turbulence conditions, QBERs <7% occur within about 45 deg of zenith. In many cases, QBER values for the FS and SMF are similar. This is most likely due to the competing effects of the increased noise filtering and reduced transmission introduced by the SMF.

Figure 8 shows results calculated assuming a daytime sky radiance value of $H_b = 100$ W/(m^2 sr μm), a factor of 4 larger than the daytime scenario summarized in the preceding figure. QBERs calculated with tracking only are unacceptably large for all cases shown. With AO however, QBERs are observed in relatively benign territory within 60 deg of zenith under moderate 1xHV$_{5/7}$ turbulence conditions and within about 40 deg under stronger 2xHV$_{5/7}$ turbulence conditions.

5.4 *Secure Key Rates for the Vacuum-Plus-Weak-Decoy-State QKD Protocol*

This section considers secure key generation rates as a metric for quantum channel performance. Secure key rates are calculated for a decoy-state QKD protocol implemented over a satellite-Earth channel.[1] The secure key generation rate per signal state, or secret bit yield, is given by[30]

$$R \geq q\{-Q_\mu f(E_\mu) H_2(E_\mu) + Q_1[1 - H_2(e_1)]\}, \tag{7}$$

where the protocol efficiency q is ½ for the BB84 protocol, μ is the mean photon number of the signal states, Q_μ is the gain of the signal states, E_μ is the overall QBER, Q_1 is the gain of the single-photon states, e_1 is the error rate of single photon states, $f(E_\mu)$ is the bidirectional error correction efficiency, and H_2 is the Shannon binary entropy function. The gain of the signal states is given by

$$Q_\mu = Y_0 + 1 - e^{-\eta\mu}, \tag{8}$$

where Y_0 is the background detection probability, $1 - e^{-\eta\mu}$ is the signal detection probability, and η is the efficiency of signal photon transmission and detection. The lower bound for the gain of the single-photon states is given by

$$Q_1 = \frac{\mu^2 e^{-\mu}}{\mu\nu - \nu^2}\left(Q_\nu e^{\nu} - Q_\mu e^{\mu}\frac{\nu^2}{\mu^2} - \frac{\mu^2 - \nu^2}{\mu^2} Y_0\right), \tag{9}$$

where ν denotes the mean photon number for the weak decoy state, $\nu < \mu$, and Q_ν is the gain of the weak decoy state given by substituting ν for μ in Eq. (8). The upper bound of e_1 is given by

$$e_1 = \frac{E_\nu Q_\nu e^\nu - e_0 Y_0}{Y_1 \nu}, \tag{10}$$

where Y_1 is the lower bound for the yield of the single-photon states given by

$$Y_1 = \frac{\mu}{\mu\nu - \nu^2}\left(Q_\nu e^\nu - Q_\mu e^\mu \frac{\nu^2}{\mu^2} - \frac{\mu^2 - \nu^2}{\mu^2} Y_0\right). \tag{11}$$

5.5 *Secure Key Rate Simulation Results*

Secure key rates are calculated assuming a 10-MHz source and a decoy-state mean photon number of $\nu = 0.05$. The efficiency of error correction $f(E_\mu)$ is taken to be a constant value of 1.22, the commonly used value associated with Cascade error correction. Rates are calculated from Eq. (7) with the source rate applied as a multiplicative factor. Results are summarized in Figs. 9–11 as average values over all frames across the 10 realizations of turbulence. Average rates of secure key generation are calculated for 400- and 800-km satellite altitudes and $1\text{x}HV_{5/7}$, $2\text{x}HV_{5/7}$, and $3\text{x}HV_{5/7}$ atmospheric turbulence profiles. Plots (a) through (f) show the results as a function of ground-station pointing angle in correspondence to the QBER plots in Figs. 6–8.

Figure 9 shows results calculated assuming a nighttime sky radiance of $H_b = 1.5 \times 10^{-2}$ W/(m^2 sr μm). With tracking only, secure key generation is possible over a range of elevation angles and turbulence conditions. For the case of the SMF shown as solid circles, this includes nonzero key rates where the average QBERs shown in Fig. 6 exceed 7%. This results from the fact that the average QBER includes atmospheric frames where the QBER is lower than the mean. For the 800-km orbit, secure key generation is possible but over a more limited range of sky angles and at lower rates due to increased propagation losses. Introducing AO improves the channel performance substantially. Secure key generation becomes possible within 60 deg of zenith for both orbit altitudes and all strengths of turbulence shown. Where secure key generation is possible with tracking, AO increases key rates by an order of magnitude or more.

Figure 10 shows results calculated assuming a daytime sky radiance value of $H_b = 25$ W/(m^2 sr μm). With the

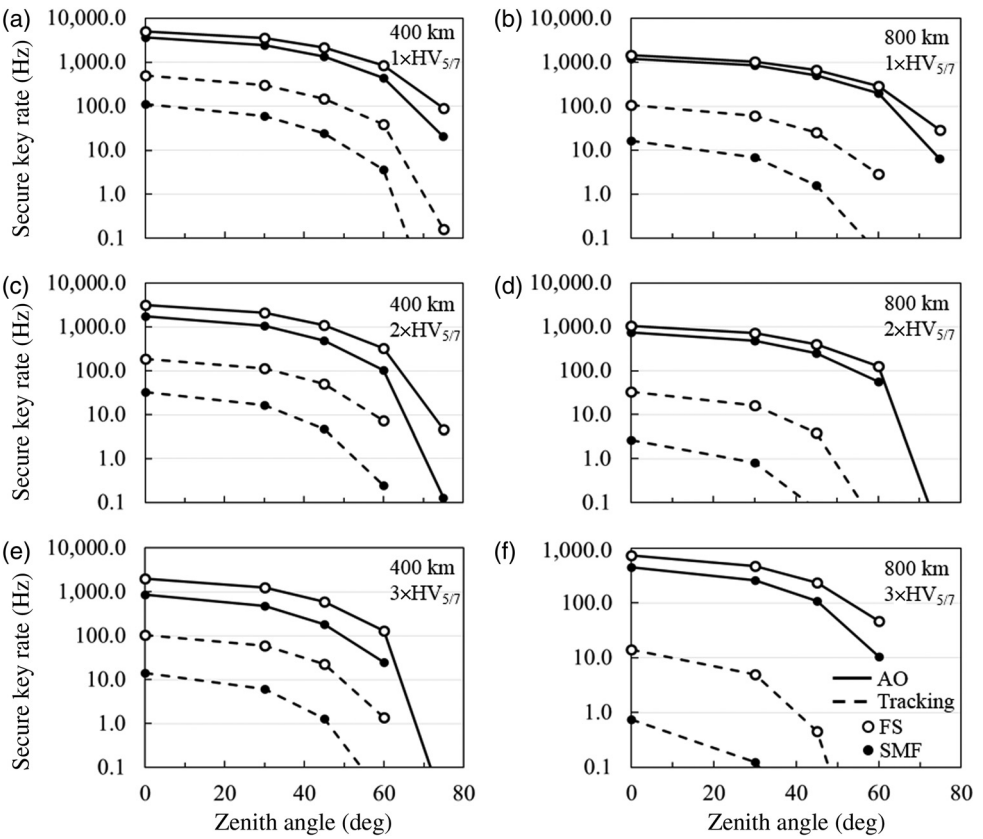

Fig. 9 Secure key generation rates versus ground-station pointing angle calculated assuming a nighttime sky radiance of $H_b = 1.5 \times 10^{-2}$ W/(m^2 sr μm) and either a circular FS, shown as open circles, or an SMF, shown as solid circles. Results calculated with tracking only are shown as dashed lines. Those calculated with higher-order AO are shown as solid lines. Combinations of turbulence strength and circular orbit altitude are given by (a) $1\text{x}HV_{5/7}$ and 400 km, (b) $1\text{x}HV_{5/7}$ and 800 km, (c) $2\text{x}HV_{5/7}$ and 400 km, (d) $2\text{x}HV_{5/7}$ and 800 km, (e) $3\text{x}HV_{5/7}$ and 400 km, and (f) $3\text{x}HV_{5/7}$ and 800 km.

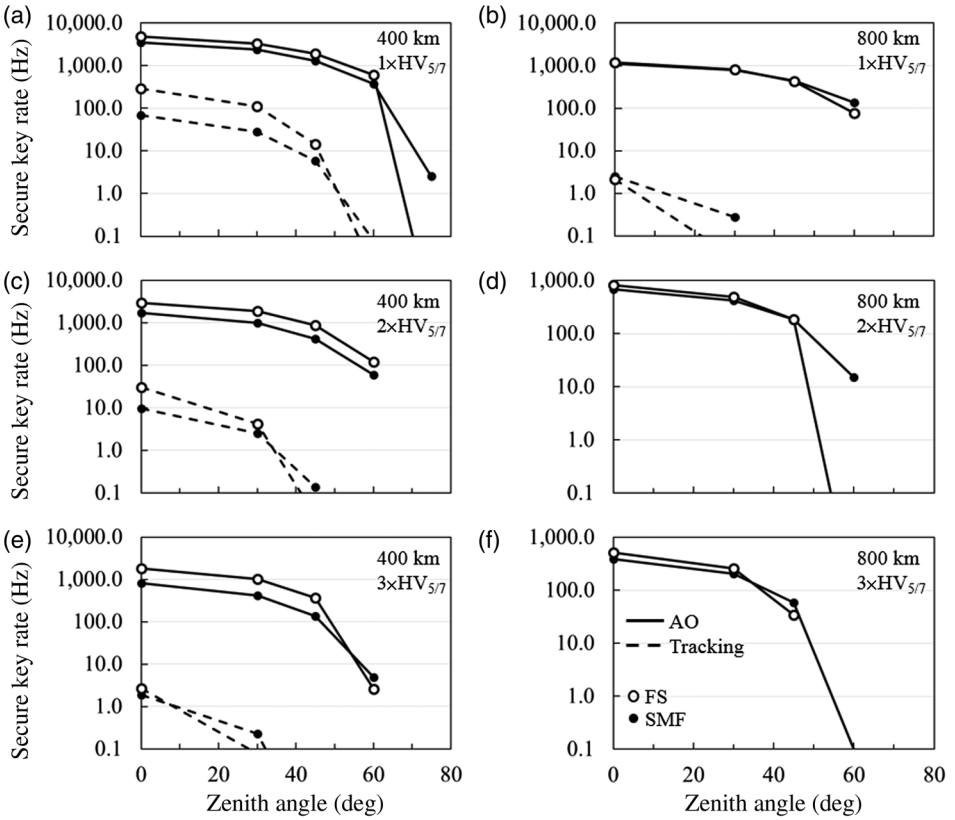

Fig. 10 Secure key generation rates versus ground-station pointing angle calculated assuming a daytime sky radiance of $H_b = 25\ \mathrm{W/(m^2\,sr\,\mu m)}$ and either a circular FS, shown as open circles, or an SMF, shown as solid circles. Results calculated with tracking only are shown as dashed lines. Those calculated with higher-order AO are shown as solid lines. Combinations of turbulence strength and circular orbit altitude are given by (a) $1\mathrm{xHV}_{5/7}$ and 400 km, (b) $1\mathrm{xHV}_{5/7}$ and 800 km, (c) $2\mathrm{xHV}_{5/7}$ and 400 km, (d) $2\mathrm{xHV}_{5/7}$ and 800 km, (e) $3\mathrm{xHV}_{5/7}$ and 400 km, and (f) $3\mathrm{xHV}_{5/7}$ and 800 km.

spectral and temporal filtering conditions assumed, secure key generation is possible with tracking but primarily for the 400-km-altitude orbit and over a range of sky angles that decreases with the increasing strength of turbulence. Introducing AO improves the channel performance substantially. For the 400-km-altitude orbit, secure key generation is possible within 60 deg of zenith for all strengths of turbulence shown. For the 800-km-altitude orbit, secure key generation is possible within 40 deg of zenith for all strengths of turbulence shown. Where secure key generation is possible with tracking, AO increases key rates by 1 to 2 orders of magnitude.

Figure 11 shows results calculated assuming a daytime sky radiance value of $H_b = 100\ \mathrm{W/(m^2\,sr\,\mu m)}$. Under the conditions of $1\mathrm{xHV}_{5/7}$ turbulence and the lower 400-km orbit, secure key generation is possible with tracking but only within zenith angles of about 30 deg. Otherwise, secure key generation is only possible with AO. For the 400-km-altitude orbit, AO makes secure key generation possible within 40 deg to 60 deg of zenith depending on the strength of turbulence. For the 800-km-altitude orbit, AO makes secure key generation possible but over a more restricted range of sky angles. In strong $3\mathrm{xHV}_{5/7}$ turbulence, the reduced FOV of the SMF permits secure key generation within 45 deg of zenith where it is not possible with the FS that is matched to the diffraction-limited field angle.

6 Conclusions

Results from detailed numerical simulations of a satellite-Earth quantum channel downlink demonstrate that a 200-Hz closed-loop bandwidth AO system can substantially enhance the performance of the channel, including the case where SMFs are part of the quantum receiver system. These results are particularly timely given the emergence of quantum technologies that integrate optical waveguides and SMFs with quantum systems and the recent advancements in space-to-Earth quantum communication.[36–39] Simulations show that the small numerical apertures associated with SMFs can play an important role in daytime sky-noise filtering, but AO can be necessary for achieving significant coupling into the SMFs. While the benign conditions of nighttime sky noise may not require this level of spatial filtering and AO compensation, these technologies may be important to a robust quantum network operating amid a range of daytime sky radiances. While these simulations were performed for a discrete-variable polarization-based protocol, the inclusion of AO to increase focal-plane transmission efficiency should improve key generation rates for any QKD protocol that is compatible with phase correction.

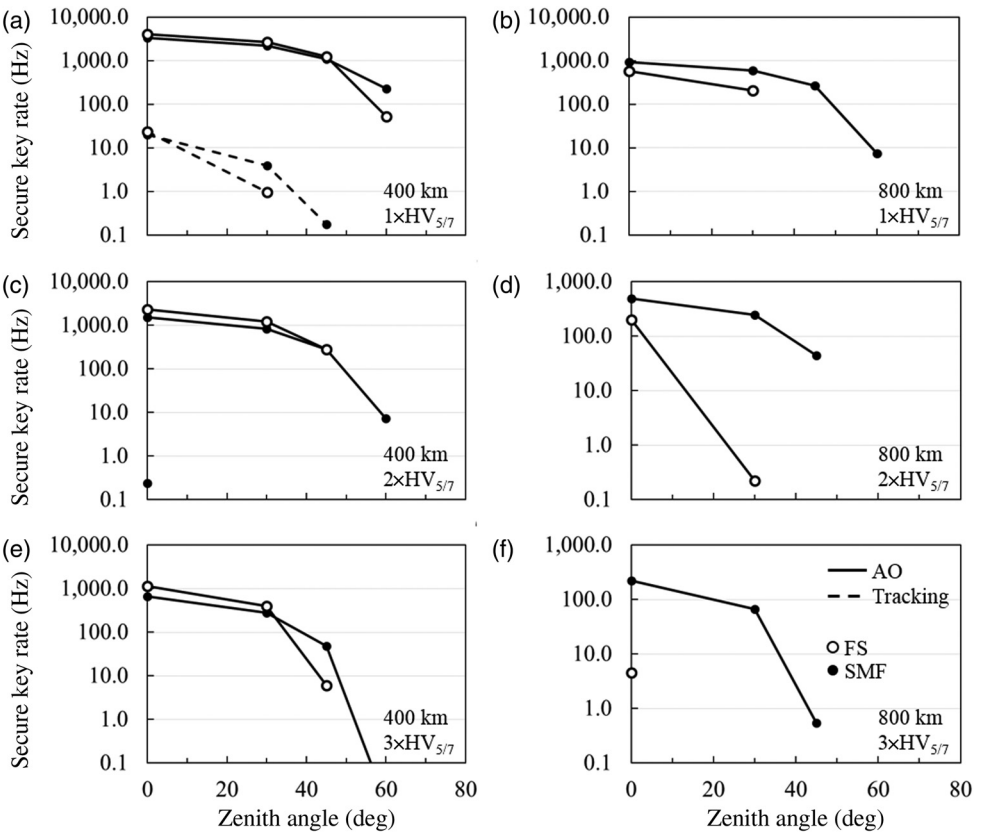

Fig. 11 Secure key generation rates versus ground-station pointing angle calculated assuming a daytime sky radiance of $H_b = 100\ \mathrm{W/(m^2\,sr\,\mu m)}$ and either a circular FS, shown as open circles, or an SMF, shown as solid circles. Results calculated with tracking only are shown as dashed lines. Those calculated with higher-order AO are shown as solid lines. Combinations of turbulence strength and circular orbit altitude are given by (a) $1\times HV_{5/7}$ and 400 km, (b) $1\times HV_{5/7}$ and 800 km, (c) $2\times HV_{5/7}$ and 400 km, (d) $2\times HV_{5/7}$ and 800 km, (e) $3\times HV_{5/7}$ and 400 km, and (f) $3\times HV_{5/7}$ and 800 km.

Appendix A: Single-Mode Optical Fiber Coupling Efficiency for the Case of a Diffraction-Limited Plane Wave

To calculate the coupling efficiency into an SMF, it is first necessary to define an optimum relationship between the size of the SMF mode and a characteristic size of the optical field. In the analysis that follows, that relationship is defined with respect to a diffraction-limited optical field at the focus. This section reviews an analytic treatment by Ruilier[40] that defines this relationship.

Consider a planar wavefront at wavelength λ incident upon a circular lens of diameter D and focal length f as illustrated in Fig. 12. The amplitude distribution at the focus is given by the Airy amplitude function

$$F_{\mathrm{Airy}} = 2\frac{J_1\left(\pi\frac{D}{\lambda f}r\right)}{\pi\frac{D}{\lambda f}r}. \tag{12}$$

A.1 Gaussian Fiber-Mode Approximation

Consider an SMF located in the focal plane of the lens. The SMF propagates the fundamental mode F_{01}. At the entrance of the fiber, the complex field mode can be approximated as a Gaussian

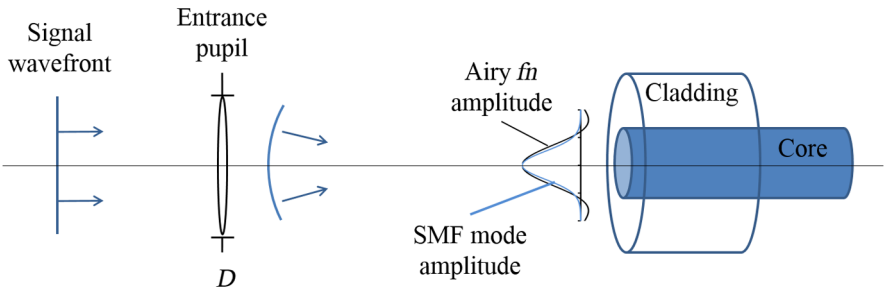

Fig. 12 Schematic illustrating a planar wavefront incident upon a lens of diameter D and focal length f brought to a focus at the entrance of a single-mode fiber. The illustration compares the amplitude distribution of the focused light with that of the fiber mode.

$$F_{01} \approx e^{-\left(\frac{r}{\omega_0}\right)^2}, \tag{13}$$

where r is the radial coordinate in the focal plane and ω_0 is the radius at the $1/e$ point of the Gaussian amplitude function. The power coupling efficiency into the fiber mode is given by the overlap integral between the optical field of Eq. (12) and the SMF mode of Eq. (13) as

$$\rho_\alpha(\beta) = 2\left\{\frac{e^{-\beta^2}[1 - e^{\beta^2(1-\alpha^2)}]}{\beta\sqrt{(1-\alpha^2)}}\right\}^2, \tag{14}$$

where

$$\beta = \frac{\pi}{2}\frac{D}{f}\frac{\omega_0}{\lambda}, \tag{15}$$

and α is the size of a central obscuration as a fraction of the pupil size. If there is no central obscuration, then the power coupling efficiency is

$$\rho(\beta) = 2\left(\frac{e^{-\beta^2} - 1}{\beta}\right)^2. \tag{16}$$

The power coupling efficiency given by Eq. (14) is plotted in Fig. 13 for three cases of a central obscuration. For the case of no obscuration, the power coupling efficiency attains a maximum value of about 81% when $\beta = 1.12$. For central obscurations of 20% and 50%, the power coupling efficiency attains maximum values of 74% and 46% when $\beta = 1.07$ and 0.92, respectively. In practice, Fresnel reflections introduce additional losses. For a given central obscuration, optimized value of β, wavelength, and fiber mode size, Eq. (15) can be solved to determine the lens diameter and focal length that optimize the coupling efficiency.

The optimum mode radius, expressed in terms of the wavelength, focal length, and lens diameter, is

$$\omega_0 = \frac{2\beta}{\pi}\frac{\lambda f}{D}. \tag{17}$$

Substituting the above equation into Eq. (13), the fiber mode can be written as a function of $Dr/\lambda f$

$$F_{01} = e^{-\left(\frac{\pi}{2\beta}\frac{D}{\lambda f}r\right)^2}. \tag{18}$$

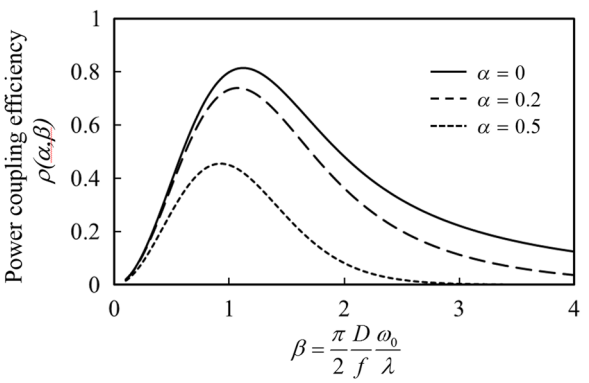

Fig. 13 Power coupling efficiency for a planar wavefront focused into an SMF for several cases of central obscuration.

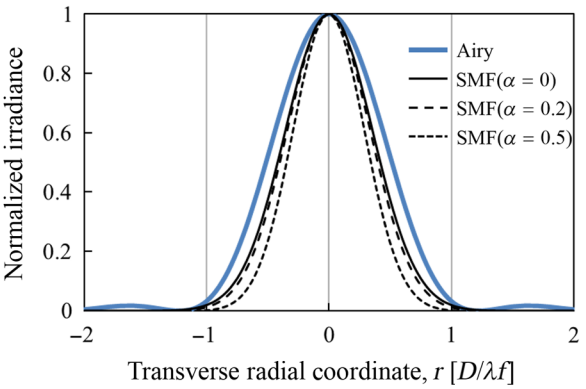

Fig. 14 Irradiance distributions of Gaussian fiber modes and the Airy function as a function of the transverse radial coordinate for the case of optimum mode overlap with three values of central obscuration size.

With this substitution, it is possible to write the optimized Gaussian fiber mode and the diffraction-limited Airy irradiance distribution as a function of $Dr/\lambda f$ as shown in Eqs. (19) and (20) and plotted in Fig. 14 for several values of α

$$I_{\mathrm{SMF01}} = e^{-2\left(\frac{\pi}{2\beta}\frac{D}{\lambda f}r\right)^2}, \tag{19}$$

$$I_{\mathrm{Airy}} = 4\left[\frac{J_1\left(\pi\frac{D}{\lambda f}r\right)}{\pi\frac{D}{\lambda f}r}\right]^2. \tag{20}$$

The diffraction-limited Airy irradiance function is plotted in blue. The irradiance distribution for the SMF mode for the case of no central obscuration, $\alpha = 0$ with $\beta = 1.12$, is shown as a black solid line. The case of a 20% obscuration, $\alpha = 0.2$ with $\beta = 1.07$, is shown as a dashed black line, and the case of a 50% obscuration, $\alpha = 0.5$ with $\beta = 0.92$, is shown as a dotted black line. As the size of the central obscuration increases, the size of the optimum fiber mode decreases.

Acknowledgments

The authors gratefully acknowledge Thomas Jennewein, Institute for Quantum Computing and Department of Physics and Astronomy, University of Waterloo, for suggesting this analysis and Fredrik Fatemi, Army Research Laboratory, for discussions regarding SMF interfaces to atomic systems. This work was supported by the Air Force Office of Scientific Research and the Office of the Secretary of Defense ARAP QSEP program.

References

1. M. T. Gruneisen et al., "Adaptive spatial filtering of daytime sky noise in a satellite quantum key distribution downlink receiver," *Opt. Eng.* **55**(2), 026104 (2016).
2. M. Peev et al., "The SECOQC quantum key distribution network in Vienna," *New J. Phys.* **11**, 075001 (2009).
3. T. Y. Chen et al., "Metropolitan all-pass and inter-city quantum communication network," *Opt. Express* **18**(26), 27217 (2010).
4. P. Solano et al., "Optical nanofibers: a new platform for quantum optics," arxiv:1703.10533 (2017).
5. F. K. Fatemi et al., "Near-field measurement of modal interference in optical nanofibers for sub-Angstrom radius sensitivity," *Optica* **4**, 157–162 (2017).

6. E. Vetsch et al., "Optical interface created by laser-cooled atoms trapped in the evanescent field surrounding an optical nanofiber," *Phys. Rev. Lett.* **104**, 203603 (2010).
7. S. Miki et al., "High performance fiber-coupled NbTiN superconducting nanowire single photon detectors with Gifford-McMahon cryocooler," *Opt. Express* **21**(8), 10208–10214 (2013).
8. F. Marsili et al., "Detecting single infrared photons with 93% system efficiency," *Nat. Photonics* **7**(3), 210–214 (2013).
9. M. Sarovar et al., "Silicon nanophotonics for scalable quantum coherent feedback networks," *EPJ Quantum Technol.* **3**, 14 (2016).
10. Y. Dikmelik and M. Davidson, "Fiber-coupling efficiency for free-space optical communication through atmospheric turbulence," *Appl. Opt.* **44**(23), 4946–4952 (2005).
11. J. Ma et al., "Statistical model of the efficiency for spatial light coupling into a single-mode fiber in the presence of atmospheric turbulence," *Appl. Opt.* **54**(31), 9287–9293 (2015).
12. T. Weyrauch et al., "Fiber coupling with adaptive optics for free-space optical communication," *Proc. SPIE* **4489**, 177–184 (2002).
13. M. Chen, C. Liu, and H. Xian, "Experimental demonstration of single-mode-fiber coupling over relatively strong turbulence with adaptive optics," *Appl. Opt.* **54**(29), 8722–8726 (2015).
14. M. W. Wright et al., "Adaptive optics correction into single mode fiber for a low Earth orbiting space to ground optical communication link using the OPALS downlink," *Opt. Express* **23**(26), 033705 (2015).
15. M. T. Gruneisen, M. B. Flanagan, and B. A. Sickmiller, "Modeling satellite-Earth quantum channel downlinks with adaptive-optics coupling to single-mode fibers," *Proc. SPIE* **10442**, 104420E (2017).
16. R. J. Hughes et al., "Practical free-space quantum key distribution over 10 km in daylight and at night," *New J. Phys.* **4**, 43 (2002).
17. R. Ursin et al., "Entanglement-based quantum communication over 144 km," *Nat. Phys.* **3**, 481–486 (2007).
18. X. S. Ma et al., "Quantum teleportation over 143 km using active feed-forward," *Nature* **489**, 269–273 (2012).
19. D. L. Fried, "Optical resolution through a randomly inhomogeneous medium for very long and very short exposures," *J. Opt. Soc. Am.* **56**, 1372–1379 (1966).
20. F. Roddier, *Progress in Optics*, Chapter 5, Vol. **XIX**, pp. 281–376, North-Holland (1981).
21. M. Sarazin and F. Roddier, "The ESO differential image motion monitor," *Astron. Astrophys.* **227**, 294–300 (1990).
22. R. K. Tyson, *Principles of Adaptive Optics*, Chapter 2, pp. 29–31, Academic Press, London, United Kingdom (1991).
23. D. J. Link, "Comparison of the effects of near-field and distributed atmospheric turbulence on the performance of an adaptive optics system," *Proc. SPIE* **2120**, 87–94 (1994).
24. D. J. Link, "Simulation of laser guidestar adaptive optics systems," *Proc. SPIE* **2375**, 30–40 (1995).
25. "WaveTrain anchoring and validation," https://mza.com/doc/wavetrain/anchor/index.htm (16 December 2015).
26. J. D. Schmidt, *Numerical Simulation of Optical Wave Propagation with Examples in MATLAB*, pp. 1–195, SPIE Press, Bellingham, Washington (2010).
27. D. G. Voelz, *Computational Fourier Optics: A MATLAB Tutorial*, pp. 1–229, SPIE Press, Bellingham, Washington (2011).
28. M. C. Roggemann and B. M. Welsh, *Imaging Through Turbulence*, CRC Press, New York (1996).
29. R. Q. Fugate, *Handbook of Optics: Classical Optics, Vision Optics, X-Ray Optics*, Chapter 1, 2nd ed., Vol. **3**, McGraw-Hill, New York (2001).
30. X. Ma et al., "Practical decoy state for quantum key distribution," *Phys. Rev. A* **72**(1), 012326 (2005).
31. E. L. Miao et al., "Background noise of satellite-to-ground quantum key distribution," *New J. Phys.* **7**, 215 (2005).
32. M. T. Gruneisen et al., "Modeling daytime sky access for a satellite quantum key distribution downlink," *Opt. Express* **23**(18), 23924 (2015).
33. M. Toyoshima et al., "Polarization measurements through space-to-ground atmospheric propagation paths by using a highly polarized laser source in space," *Opt. Express* **17**(25), 22333–22340 (2009).
34. H. T. Friis, "Introduction to radio and radio antennas," *IEEE Spectrum* **8**(4), 55–61 (1971).
35. S. B. Alexander, *Optical Communication Receiver Design*, Chapter 2, p. 37, SPIE Press, Bellingham, Washington (1997).
36. J. Yin et al., "Satellite-based entanglement distribution over 1200 kilometers," *Science* **356**, 1140–1144 (2017).
37. J. G. Ren et al., "Ground to satellite quantum teleportation," *Nature* **549**(7670), 70–73 (2017).
38. S. K. Liao et al., "Satellite-to-ground quantum key distribution," *Nature* **549**(7670), 43–47 (2017).
39. H. Takenaka et al, "Satellite-to-ground quantum-limited communication using a 50-kg-class micro-satellite," *Nat. Photonics* **11**, 502–508 (2017).
40. C. Ruilier, "A study of degraded light coupling into single-mode fibers," *Proc. SPIE* **3550**, 319–329 (1998).

Mark T. Gruneisen received his PhD in optics from the University of Rochester, Rochester, New York, in 1988. He is the principal investigator for quantum communication research in the Air Force Research Laboratory's Directed Energy Directorate. He is a fellow of SPIE, chair for the SPIE Quantum Technologies and Quantum Information Science Conference, and corecipient of the SPIE 2004 Rudolf Kingslake Medal.

Michael B. Flanagan is an optical research scientist with Leidos. He earned his doctorate in applied mathematics from Texas A&M University in 2002 and has been working on adaptive-optics research and analysis for the last 13 years.

Brett A. Sickmiller received his PhD in engineering physics from the University of Virginia, Charlottesville, Virginia, in 2008. He is currently a principal systems engineer at Raytheon. Previously, he worked as an optical research analyst for Leidos supporting optical and quantum communications research in the Air Force Research Laboratory's Directed Energy Directorate.